ScienceDirect

Discrete Wavelet Transform

Related terms:

Wavelet, Haar Wavelet, Wavelet Packets, Analysis of Variance, Wavelet Transforms, High-Pass Filter, Low-Pass Filter, Multivariate

Time Series Analysis: Methods and Applications

Donald B. Percival, Debashis Mondal, in Handbook of Statistics, 2012

1 Introduction

The discrete wavelet transform (DWT), as formulated in the late 1980s by Daubechies (1988), Mallat (1989a,b,c), and others, has inspired extensive research into how to use this transform to study time series. One focus of this research has been on the wavelet variance (also called the wavelet spectrum). The wavelet variance decomposes the variance of a time series and, hence, provides an analysis of variance (ANOVA). The most widely used ANOVA technique in time series analysis is spectral analysis, which involves the Fourier-based spectral density function (SDF). The ANOVA that the wavelet variance provides is in many ways similar to that afforded by the SDF (Li and Oh, 2002); however, from a practitioner's point of view, there are key differences. The SDF is a decomposition of variance across a continuum of Fourier frequencies. Each component in the decomposition reflects the degree to which a time series resembles a sinusoid with a particular frequency. The wavelet variance differs in that it is a decomposition across a discrete set of scales. Roughly speaking, a scale is an interval (or span) of time over which a time series is averaged. The strength of each component in the decomposition measures how much variability there is between adjacently located averages associated with a particular scale. The concept of scale is distinct from that of period (the inverse of frequency). Both are measured in the same units, but period does not involve averaging. Although it is possible to estimate an SDF indirectly via the wavelet variance (Tsakiroglou and Walden, 2002), the different interpretations that frequency and scale have make the ANOVA afforded by the wavelet variance more appealing than the one given by the SDF for interpreting certain time series. Examples of applications that have made use of the wavelet variance are extensive and include time series related to electroencephalographic sleep state patterns of infants (Chiann and Morettin, 1998), frequency instability of atomic clocks (Greenhall et al., 1999), rainfall/runoff relationships (Labat et al., 2001), variations in soil composition (Lark and Webster 2001), ocean surface waves (Massel 2001), surface albedo and temperature in desert grasslands (Pelgrum et al., 2000), heart rate variability (Pichot et al., 1999), stochastic fluctuations on accreting binary stars (Scargle et al., 1993), solar coronal activity (Rybák and Dorotovič 2002), and the El Niño–Southern Oscillation (Torrence and Compo 1998). In addition, in contrast to the Fourier transform, the DWT is localized in time, and hence, the wavelet variance can be readily adapted for exploring processes that are locally stationary with time-varying SDFs (Nason et al., 2000) and for detecting inhomogeneities in time series (Whitcher et al., 2002).

The intent of this chapter is to provide a basic introduction to the wavelet variance, with an emphasis on its interpretation, its statistical properties, and some recent extensions to the basic methodology. We start with an overview of the maximal overlap DWT (MODWT), which is the version of the DWT of most interest for formulating the wavelet variance (Section 2). The MODWT leads to a basic ANOVA of a time series, which we describe in Section 3. If we assume that the time series under analysis is a realization of an intrinsically stationary process (as defined in Section 4), we can define a theoretical wavelet variance and regard the descriptive statistics discussed in Section 3 as basic estimators of this variance. We discuss the fundamental statistical theory behind estimators of the wavelet variance in Section 5, following which we discuss estimators intended to handle special circumstances (gappy time series in Section 6.1 and series with aberrant observations in Section 6.2). We then describe two wavelet-based methodologies in Section 7, one for deducing the presence of power-law dependence in a time series and the other for defining a characteristic scale. In both cases, the statistics that arise are qualitatively similar in that they combine wavelet variance estimates together across adjacent scales. We devote the penultimate Section (8) to five real-world examples illustrating the methodology discussed in previous sections (two of these examples serve to briefly compare Fourier-based spectral analysis with the analysis afforded by the wavelet variance; see also Faÿ et al. (2009)). We close with some concluding remarks in Section 9.

Read full chapter

Time Series Analysis and Mining

Yangchang Zhao, in R and Data Mining, 2013

8.5.2 Classification with Extracted Features

Next, we use DWT (Discrete Wavelet Transform)(Burrus et al., 1998) to extract features from time series and then build a classification model. Wavelet transform provides a multi-resolution representation using wavelets. An example of Haar Wavelet Transform, the simplest DWT, is available at `http://dmr.ath.cx/gfx/haar/`. Another popular feature extraction technique is Discrete Fourier Transform (DFT) (Agrawal et al., 1993).

An example on extracting DWT (with Haar filter) coefficients is shown below. Package *wavelets* (Aldrich, 2010) are used for discrete wavelet transform. In the package, function `dwt(X, filter, n.levels, ...)` computes the discrete wavelet transform coefficients, where `X` is a univariate or multivariate time series, `filter` indicates which wavelet filter to use, and `n.levels` specifies the level of decomposition. It returns an object of class `dwt`, whose slot `W` contains wavelet coefficients and `V` contains scaling coefficients. The original time series can be reconstructed via an inverse discrete wavelet transform with function `idwt()` in the same package. The produced model is shown in Figure 8.10.

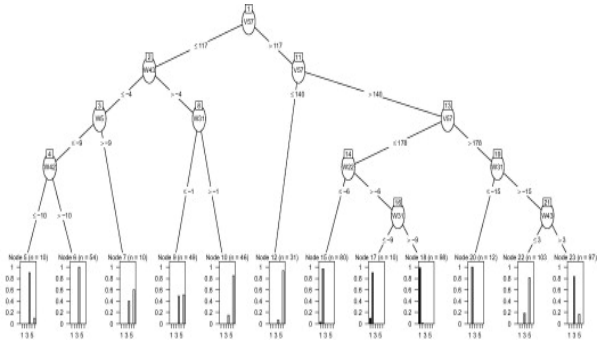

Figure 8.10. Decision tree with DWT.

```
> library(wavelets)
> wtData <- NULL
> for(i in 1:nrow(sc)) {
+ a <- t(sc[i,])
+ wt <- dwt(a, filter="haar", boundary="periodic")
+ wtData <- rbind(wtData, unlist(c(wt@W, wt@V[[wt@level]])))
+ }
> wtData <- as.data.frame(wtData)
> wtSc <- data.frame(cbind(classId, wtData))
> # build a decision tree with DWT coefficients
> ct <- ctree(classId ~ ., data=wtSc,
 controls =ctree_control(minsplit=30, minbucket=10, maxdepth=5))
> pClassId <- predict(ct)
> table(classId, pClassId)
```

	pClassId					
classId	1	2	3	4	5	6
1	97	3	0	0	0	0
2	1	99	0	0	0	0
3	0	0	81	0	19	0
4	0	0	0	63	0	37
5	0	0	16	0	84	0
6	0	0	0	1	0	99

```
>(sum(classId==pClassId))/ nrow(wtSc)
[1] 0.8716667
> plot(ct, ip_args=list(pval=FALSE), ep_args=list(digits=0))
```

Read full chapter

URL: https://www.sciencedirect.com/science/article/pii/B9780123969637000088

Volume 3

D.A. Donald, ... D. Coomans, in Comprehensive Chemometrics, 2009

3.23.2.6 Inverse Transforms: Discrete Wavelet and Wavelet Packet

If all the resulting bands from a DWT or WPT are known, i.e., final DWT or WPT coefficients, then the inverse transform will result in recreation of the original data matrix **X**. However, it is common practice to retain only one band of coefficients, as the main purpose of both the DWT and the WPT is to reduce the dimensionality of the data set. For the DWT, the band $\mathbf{X}^{[l]}(0)$ is retained, whereas the band $\mathbf{X}^{[l]}(t)$ is maintained for the WPT, where *l* is the number of times the wavelet decomposition is applied. As only one band is retained for the DWT and the WPT, the resulting inverse transformation $\mathbf{X}^{*}$ will be an approximation of **X**.

Both the DWT and the WPT consist of iterative applications of the wavelet transform. It is not surprising that the inverse WPT and DWT transformations consist of iterative applications of the inverse wavelet transform. Noting that

$$\mathbf{W}^{[i]\mathrm{T}}\mathbf{W}^{[i]} = \mathbf{I}, \quad i = 1, \ldots, l \tag{23}$$

Equations (21) and (22) can be rearranged to give

$$\mathbf{X}^{[i-1]}(f) = \mathbf{W}^{[i-1]\mathrm{T}}\mathbf{X}^{[i]}(k), \quad i = 1, \ldots, l \tag{24}$$

where

$$\mathbf{X}^{[i]}(k) = \left(\mathbf{X}^{[i]}(f \times i - r), \mathbf{X}^{[i]}(f \times i - r + 1), \ldots, \mathbf{X}^{[i]}(f \times i - r + m\right.$$

$$f = \mathbf{floor}\left(\frac{j}{m}\right), \quad \begin{cases} j = 0, & \mathbf{DWT} \\ j = t, & \mathbf{WPT} \end{cases}$$

$$r = \mathbf{remainder}\left(\frac{j}{m}\right)$$

Equation (24) provides an iterative algorithm for calculating the inverse transforms for the DWT and WPT transforms. However, it may be necessary to 'pad' elements of $\mathbf{X}^{[i]}(k)$ by letting $\mathbf{X}^{(i)}(n) = \mathbf{0}$, where **0** is a matrix of zeros with the same dimensions as $\mathbf{X}^{[i]}(n)$ and $n - f \times i - r, \ldots, f \times i - r + m - 1, \neq j$. This padding may be necessary as only one band of coefficients is retained from the DWT or WPT (i.e., all the other coefficient bands are deleted).

Read full chapter

URL: https://www.sciencedirect.com/science/article/pii/B9780444527011000338

Logarithmic Wavelets

Laurent Navarro, ... Michel Jourlin, in Advances in Imaging and Electron Physics, 2014

4.4.1 Definitions

Since the main purpose of this chapter is to propose a wavelet logarithmic framework for image processing, it is more interesting to present directly the 2-D DWT as it is intrinsically related to image processing. More particularly, MRA combines different image processing techniques to decompose an image function *f* on a wavelet basis. In this section, the 2-D discrete logarithmic wavelet transform is developed. As its linear equivalent, sub-band coding, pyramidal image processing, and quadrature mirror filtering are used.

The (linear) 2-D DWT was presented previously in Figures 13 and 14. As for the latter, the 2-D discrete logarithmic wavelet transform is computed by taking into account the two functions:

- A scaling function $\varphi_{\triangle}$ associated with a multiresolution $V_{j\in\mathbb{Z}}$ of $L^2(\mathbb{R})$
- A wavelet $\zeta_{\triangle}$ whose dilated and translated form $2^{\frac{j}{2}}\zeta\left(2^j t - n\right)$ is an orthonormal basis of $L^2(\mathbb{R}) = \oplus_j W_j$

The generic expression of the wavelet is:

$$\zeta^{k}_{\triangle j,n}(x, y) = 2^j \zeta^{k}_{\triangle}\left(2^j x - n_1, 2^j y - n_2\right) \tag{73}$$

for $1 \leq k \leq 3$.

The directional wavelets are obtained by the product of a 1-D scaling function and the corresponding wavelet function:

$$\begin{aligned}\zeta_{\Delta}^{1}(x,y) &= \varphi_{\Delta}(x) \vartriangle \zeta_{\Delta}(y)\\ \zeta_{\Delta}^{2}(x,y) &= \zeta_{\Delta}(x) \vartriangle \varphi_{\Delta}(y)\\ \zeta_{\Delta}^{3}(x,y) &= \zeta_{\Delta}(x) \vartriangle \zeta_{\Delta}(y),\end{aligned} \tag{74}$$

where $\zeta_{\Delta}^{1} = \zeta_{\Delta}^{H}, \zeta_{\Delta}^{2} = \zeta_{\Delta}^{V}, \zeta_{\Delta}^{3} = \zeta_{\Delta}^{D}$ allow the detection of the horizontal, vertical, and diagonal variations, respectively.

The representation of the logarithmic wavelet coefficients (Figure 11) is identical to the linear one, as only the amplitudes of the wavelet coefficients are logarithmic.

The directional wavelets $\zeta_{\Delta\ j,n}^{1}, \zeta_{\Delta\ j,n}^{2}, \zeta_{\Delta\ j,n}^{3}$ form an orthonormal basis of the subspace of details $W_j^2 = (V_{j \otimes \Delta} W_j) \oplus (W_{j \otimes \Delta} V_j) \oplus (W_{j \otimes \Delta} W_j)$ at scale j, with $L^2(\mathbb{R}^2) = \oplus_j W_j^2$.

The notation $\otimes\Delta$ designs a logarithmic tensor product. The whole image f decomposes as

$$f(x,y) = \sum_{i,j,k} d_{j,k}^{i} 2^{j} \vartriangle \zeta_{\Delta\ j,k}^{i}(x,y), \tag{75}$$

and

$$d_{j,k}^{i} = \left\langle \zeta_{\Delta\ j,k}^{i} \middle| f\left(x,y\right) \right\rangle_{\Delta} \tag{76}$$

is the discrete wavelet of the considered image f, as a function of the three discrete variables i, j, and k.

The fast 2-D logarithmic wavelet transform is calculated with the recursive application of the filter bank shown in Figure 13, with logarithmic wavelets and operators.

Similarly, the structure of the inverse 2-D log, arithmic discrete wavelet transform leading to the synthesis of the considered image is based on a logarithmic filter bank (Figure 14).

Read full chapter

URL: https://www.sciencedirect.com/science/article/pii/B9780128002650000023

Stochastic Multiresolution Models for Turbulence

B. Whitcher, ... T.J. Hoar, in Recent Advances and Trends in Nonparametric Statistics, 2003

2.1 Multiresolution Analysis

To simplify the vortex dynamics within a given realization of a vorticity field, we rely on the two-dimensional discrete wavelet transform (2D DWT) and assume the vorticity field $\zeta(\mathbf{x})$ has finite energy; i.e., $\int \zeta^2(\mathbf{x})\,d\mathbf{x} < \infty$. Let ϕ be a scaling function and ψ be the corresponding wavelet generating an orthonormal basis on $L^2(\mathbb{R})$ and define the three separable wavelets

$$\psi^{h}(x_1,x_2) = \phi(x_1)\psi(x_2), \quad \psi^{v}(x_1,x_2) = \psi(x_1)\phi(x_2), \quad \psi^{d}(x_1,x_2) = \psi(x_1)\psi(x_2) \tag{1}$$

corresponding to horizontal, vertical and diagonal directions, respectively. More information concerning the interpretation of "spatial directions" captured by the separable wavelet transform may be found in Section 2.2. The separable scaling function $\phi(x_1, x_2) = \phi(x_1)\phi(x_2)$ is associated with the approximation space. For $m \in \{h, v, d\}$, let

$$\psi_{j,k,l}^{m}(x_1,x_2) = \frac{1}{2^j}\psi^{m}\left(\frac{x_1 - 2^j k}{2^j}, \frac{x_2 - 2^j l}{2^j}\right),$$

such that

$$\left\{\psi_{j,k,l}^{h}(x_1,x_2), \psi_{j,k,l}^{v}(x_1,x_2), \psi_{j,k,l}^{d}(x_1,x_2)\right\}_{(j,k,l)\in\mathbb{Z}^3}$$

is an orthonormal basis of $L^2(\mathbb{R}^2)$. The triplet (j, k, l) denotes the jth wavelet scale at the spatial position (k, l). In practice the depth of the 2D DWT is determined by the finite dimension $M \times N$ of $\zeta(\mathbf{x})$, such that $1 \leq j \leq J = \lfloor \log_2 \min\{M, N\} \rfloor$. Efficient implementation of the separable 2D DWT is performed via a series of convolutions and subsampling [3, Sec. 7.7].

Whereas it would be most efficient to represent the vorticity field using a decimated transform such as the 2D DWT, we find it advantageous to utilize the 2D maximal overlap DWT (2D MODWT). Unlike the orthonormal 2D DWT, the 2D MODWT produces a redundant non-orthogonal transform. The reason for this discrepancy is that the 2D MODWT does not subsample in either dimension, it

only filters the original image. The advantages are that the transform is translation invariant to integer shifts in space and it reduces artifacts caused by the choice of a specific wavelet filter.

Let $\overline{\phi} = \phi/\sqrt{2}$ and $\overline{\psi} = \psi/\sqrt{2}$ be rescaled versions of the scaling and wavelet functions. The three separable wavelet functions associated with spatial directions $m \in \{h, v, d\}$ are now

$$\overline{\psi}^m_{j,k,l}(x_1, x_2) = \frac{1}{2^{2j}} \psi^m \left(\frac{x_1 - k}{2^j}, \frac{x_2 - l}{2^j} \right).$$

Hence, each level in the transform will have the same spatial dimension as the original field ($M \times N$) and represent a redundant set of wavelet coefficients. The 2D MODWT begins with the original vorticity field $\zeta(\mathbf{x})$, and at all scales we denote $\overline{v}_j(k,l) = \langle \zeta, \phi_{j,k,l} \rangle$ and $\overline{w}_j(k,l) = \left\langle \zeta, \psi^m_{j,k,l} \right\rangle$ $m \in \{h, v, d\}$ where $\langle x, y \rangle$ is the two-dimensional inner product of $x(\cdot,\cdot)$ and $y(\cdot,\cdot)$. The vorticity field $\zeta(\mathbf{x})$ may now be decomposed into $3J + 1$ sub-fields,

$$\left[\left\{ \overline{w}^h_j, \overline{w}^v_j, \overline{w}^d_j \right\}_{1 \le j \le J}, \overline{v}_J \right]; \tag{2}$$

three fields of wavelet coefficients corresponding to distinct spatial directions and one field containing the scaling coefficients at the final level. The scaling (approximation) field for level j may be obtained from the four fields at level $j + 1$ via

$$\overline{v}_j(k,l) = \left\langle \overline{v}_{j+1}, \phi^*_{j,k,l} \right\rangle + \sum_m \left\langle \overline{w}^m_{j+1}, \psi^{m*}_{j,k,l} \right\rangle. \tag{3}$$

The 2D MODWT *multiresolution analysis* (MRA) of the vorticity field is an additive decomposition given by recursively applying (3) over all j; i.e.,

$$\zeta(x_1, x_2) = \left\langle \overline{v}_J, \phi^*_{J,x_1,x_2} \right\rangle + \sum_{j=1}^{J} \sum_m \left\langle \overline{w}^m_j, \psi^{m*}_{j,x_1,x_2} \right\rangle = \overline{a}_J(x_1, x_2) + \sum_{j=1}^{J} \sum_m$$

where $\overline{a}_J(x_1, x_2)$ is the wavelet approximation field and $\overline{d}^m_j(x_1, x_2)$ is the wavelet detail field associated with the spatial direction $m \in \{h, v, d\}$. The MRA of $\zeta(\mathbf{x})$ provides a convenient way of isolating features at different scales and directions with coefficients in the spatial domain versus the wavelet domain. This is advantageous since reconstruction is now reduced from the full inverse 2D MODWT to simple addition.

Read full chapter

URL: https://www.sciencedirect.com/science/article/pii/B978044451378650034X

Multirate and Wavelet Signal Processing

In Wavelet Analysis and Its Applications, 1998

5.3.1.10 Reflections on the wavelet transform

By examining multiresolution analysis, we are ready to draw some interesting conclusions about wavelets.

1. *Concept of Scale.* The discrete wavelet transform is useful for representing the finer variations in the signal $f(t)$ at various scales. Moreover, the function $f(t)$ can be represented as a linear combination of functions that represent the variations at different scales.
2. *Localized Basis.* If a signal has energy at a particular scale concentrated in an interval in the time domain, then the corresponding coefficient has a large value. Therefore, the wavelet basis provides localization information in both the time domain as well as the scale domain.

Read full chapter

URL: https://www.sciencedirect.com/science/article/pii/S1874608X98800502

Tree-Adapted Wavelet Shrinkage

James S. Walker, in Advances in Imaging and Electron Physics, 2002

D Discrete Wavelet Analysis

The equations in (9), starting from initial data $\left\{ \alpha^M_j = f_j \right\}$, provide a discrete wavelet transform. To see how this works let us first consider the simplest case, the Haar transform.

For Haar wavelets, $N = 0$, $c_0 = c_1 = 1/\sqrt{2}$, and $d_0 = 1/\sqrt{2}, d_1 = -1/\sqrt{2}$. Equation (9) then yields the following transformation:

$$\alpha_j^{M-1} = \frac{f_{2j} + f_{2j+1}}{\sqrt{2}} \quad \beta_j^{M-1} = \frac{f_{2j} - f_{2j+1}}{\sqrt{2}} \tag{12}$$

In practice, these formulas are applied to a finite set of initial values. Let us begin with a vector $\mathbf{f} = (f_0, f_1, \ldots, f_{J-1})$, where we assume J is even. Applying Eq. (12) to **f** yields the vector

$$\left(\mathbf{a}^1 \mid \mathbf{b}^1\right) = \left(\alpha_0^{M-1}, \alpha_2^{M-1}, \ldots, \alpha_{(J-1)/2}^{M-1} \mid \beta_0^{M-1}, \beta_1^{M-1}, \ldots, \beta_{(J-1)/2}^{M-1}\right)$$

The mapping $\mathbf{f} \mapsto (\mathbf{a}^1 \mid \mathbf{b}^1)$ is the first-level Haar transform of **f**. The vector $\mathbf{a}^1$ is called the *trend* of **f**, and the vector $\mathbf{b}^1$ is called the *fluctuation* of **f**.

It is easy to see that the first-level Haar transform is orthogonal. It preserves the *energy* of vectors, as measured by sums of squares.

If J can be divided several times by 2, then several levels of Haar transform can be performed. For example, if J is divisible by 4, then **f** has a second-level Haar transform. This is found by iterating the first-level Haar transform, by applying it to the trend vector $\mathbf{a}^1$. This is just a special instance of the formulas in (9) for the Haar case.

As an example of these ideas, let us consider the following analog signal:

$$f(x) = (\sin 25\pi x)\mathbf{1}_{[0,\,0.25]}(x) + (4 + \cos 45\pi x)\mathbf{1}_{(0.25,\,0.75]}(x) + (\sin 35\pi x)\mathbf{1}_{(0.75,\,1)}(x)$$

The graph of the vector **f**, which consists of J = 16,384 samples of the signal $f(x)$ over the interval [0,1), is shown in Figure 2a. The first-level Haar transform of this signal is shown at the top of Figure 2b. The trend $\mathbf{a}^1$ is graphed over[0, 0.5) and the fluctuation $\mathbf{b}^1$ is graphed over [0.5, 1). Notice that the trend $\mathbf{a}^1$ closely resembles the original vector **f**. The trend also contains 99.992% of the energy of **f**. The fluctuation $\mathbf{b}^1$ shows only two noticeable values, which correspond to the jump discontinuities $f(x)$. Because the fluctuation contains such a small amount of energy, what little energy it has is confined mostly to these two peak values.

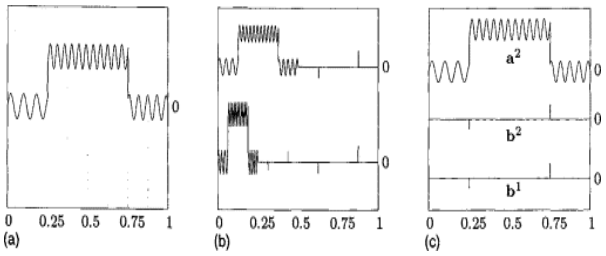

Figure 2. (a) Test signal. (b, top) First-level Haar transform, (b, bottom) Second-level Haar transform. (c, top) Second-level trend. (c, middle) Second-level fluctuation. (c, bottom) First-level fluctuation.

Similar remarks apply to the second-level transform shown in Figure 2b (bottom). This second-level transform is also displayed in Figure 2c, where each of the vectors $\mathbf{a}^2$, $\mathbf{b}^2$, and $\mathbf{b}^1$ are graphed over the interval [0,1). Comparing the graph of $\mathbf{a}^2$ with the graph of **f** clearly shows that they are closely related in form, although $\mathbf{a}^2$ has only a quarter of the values of **f**, spaced four times as far apart. The second-level trend $\mathbf{a}^2$ contains 99.990% of the energy of **f**. Notice that the fluctuations $\mathbf{b}^2$ and $\mathbf{b}^1$, when graphed over the interval [0, 1), provide excellent locators for the positions of the jump discontinuities of $f(x)$. Similar results can be found for images. However, with images, instead of jump discontinuities at isolated points, there are *edges* along curves.

For Daubechies wavelets, there are similar wavelet transformations. For example, if we use the coefficients in Eq. (8), the first-level Daub4 discrete wavelet transform is defined by*

$$\begin{aligned} \alpha_j^{m-1} &= c_0 f_{2j} + c_1 f_{2j+1} + c_2 f_{2j+2} + c_3 f_{2j+3} \\ \beta_j^{m-1} &= d_0 f_{2j} + d_1 f_{2j+1} + d_2 f_{2j+2} + d_3 f_{2j+3} \end{aligned} \tag{13}$$

These equations define an orthogonal transform $\mathbf{f} \mapsto (\mathbf{a}^1 \mid \mathbf{b}^1)$. Higher-level Daub4 transforms, as with the higher-level Haar transforms, are defined by iteration on the trend vectors $\mathbf{a}^1$, $\mathbf{a}^2$, and so forth.

One advantage of Daubechies wavelets is that the moment conditions in Eq. (3) imply corresponding discrete moment conditions on the constants $\{d_k\}$ used for generating wavelet coefficients in the discrete transform. These discrete moment conditions are (let $0^0 = 1$ to enable a single statement):

$$\sum_{k=0}^{2N+1} k^n d_k = 0 \quad n = 0, 1, \ldots, N \tag{14}$$

Given our signal model, these discrete moment conditions imply that there will be many small-magnitude wavelet coefficients. In fact, if the vector **f** consists of samples from a signal that can be closely approximated over the support of ψ_j^{m-1}

by a polynomial of degree N (as in a truncated Taylor expansion), then Eq. (14) implies that β_j^{m-1} will be approximately zero.

Notice how this last statement for wavelet coefficients of discrete signals corresponds to a similar statement made previously for wavelet coefficients of analog signals. On the basis of this correspondence, the following basic properties for the discrete Daubechies wavelet transforms (assuming our signal model) can be stated:

Energy Conservation. The wavelet transform is an orthogonal transform.

Energy Compaction. There are large numbers of small-magnitude wavelet coefficients. Most of the energy is concentrated in the trend.

Two Populations. The larger wavelet coefficients are clustered around sharp transition regions (edges in images). Smaller wavelet coefficients reside in smoother regions.

Clustering. Large-magnitude wavelet coefficients tend to have some large-magnitude coefficients located near them.

Note that the clustering property was not discussed previously. It is not difficult to see that it holds, however. It follows from the large amount of overlap of the supports of the Daubechies wavelets. Consequently, when a wavelet coefficient β_j^m is relatively large, there is a tendency for one of its neighbors β_{j-1}^m or β_{j+1}^m to be large as well.

Read full chapter

URL: https://www.sciencedirect.com/science/article/pii/S1076567002800465

Signal and Image Representation in Combined Spaces

Charles K. Chui, Chun Li, in Wavelet Analysis and Its Applications, 1998

1 Introduction

It is well known that the coefficient sequence of the Fourier series expansion of a periodic signal (or function) is often used to characterize the order of smoothness of the signal itself. This so–called Littlewood–Paley approach to wavelet series expansions (often called discrete wavelet transforms, DWT) is also well documented in the wavelet literature (see, for instance, the monograph [10] of Y. Meyer). This study, however, is within the L^p theory of wavelet analysis. Based on the pioneer work of Donoho [5], we recently developed in [2] a parallel theory of the DWT for the space C_u of bounded and uniformly continuous functions on R. The basic functions that generate the local series expansions are interpolatory wavelets, such as those of Micchelli (see [2]) and Donoho [5]; and the coefficients are functional wavelet transforms, FnWT, of the functions in C_u under investigation. The importance of the FnWT is that it reveals the local details, just as the DWT does, of the functions under investigation by using their discrete function values directly, by means of Lagrange interpolation.

This paper may be considered a continuation of our work developed in [2]. The objective here is to characterize the smoothness of functions (or signals) in $C_u \cap L^p (1 \le p \le \infty)$ in terms of the wavelet coefficients of the interpolatory wavelet series representation that are used in the process of interpolatory wavelet decompositions. This characterization will involve Besov spaces as well as Sobolev spaces. We emphasize that the important role of the duals of the interpolatory wavelets is mainly due to the property of vanishing moments to be described in Section 2. In this respect, our point of view and mathematical analysis are quite different from those in Donoho [5].

This paper is organized as follows. In Section 2 we will discuss the notion of interpolatory scaling functions, wavelets, and their duals as introduced in [2], and will describe some of their basic properties that are needed for stating and establishing our main results. Unlike the L^2 situation, the duals here are not functions in the same space as the wavelets and the original functions to be analyzed. In fact, they are distributions generated by the Dirac functional. The main results of this paper will be established in Sections 3 and 4.

Read full chapter

URL: https://www.sciencedirect.com/science/article/pii/S1874608X98800150

3-D Sparse Representations

Francois Lanusse, ... M.Jalal Fadili, in Advances in Imaging and Electron Physics, 2014

2.2 3-D Isotropic Undecimated Wavelet Transform (IUWT)

The main interest of the biorthogonal wavelet transform introduced in the previous section is its lack of redundancy: the transform of an $N \times N \times N$ cube is a cube of the same size. This property is particularly appreciable in three dimensions, as the resources needed to process a 3-D signal scale faster than for lower dimensions. However, this DWT is far from optimal for applications such as restoration (e.g., denoising or deconvolution), detection, or more generally, analysis of data. Indeed, modifications of DWT coefficients introduce a large number of artifacts in the signal after reconstruction, mainly due to the loss of translation-invariance in the DWT.

For this reason, for restoration and detection purposes, redundant transforms are generally preferred. Here, we present the 3-D version of the IUWT, which also is known as the starlet *wavelet* transform because its 2-D version is well adapted to the more or less isotropic features found in astronomical data (Starck, and Murtagh 1994); Starck, and Murtagh 2006.

The starlet transform is based on a separable isotropic scaling function:

$$\phi(x, y, z) = \phi_{1D}(x)\,\phi_{1D}(y)\,\phi_{1D}(z), \tag{16}$$

where ϕ_{1D} is a 1-D B-spline of order 3:

$$\phi_{1D}(x) = \tfrac{1}{12}\left(|x-2|^3 - 4|x-1|^3 + 6|x|^3 - 4|x+1|^3 + |x+2|^3\right). \tag{17}$$

The separability of ϕ is not a required condition, but it allows for fast computation, which is especially important for large-scale data sets in three dimensions.

Algorithm 1: The 3-D Biorthogonal Wavelet Transform

Data: An $N \times N \times N$ data cube X

Result: $W = \{w_1^1, w_1^2, \ldots, w_1^7, w_2^1, \ldots, w_J^1, \ldots w_J^7, c_J\}$ the 3-D DWT of X.

begin

$c_0 = X, J = \log_2 N$

for $j = 0$ *to* J — 1 do

Compute $c_{j+1} = \overline{h}\,\overline{h}\,\overline{h} * c_j$, downsample by a factor of 2 in each dimension.

Compute $w_{j+1}^1 = \overline{g}\overline{h}\,\overline{h} * c_j$, downsample by a factor of 2 in each dimension.

Compute $w_{j+1}^2 = \overline{g}\,\overline{g}\overline{h} * c_j$, downsample by a factor of 2 in each dimension.

Compute $w_{j+1}^3 = \overline{h}\overline{g}\overline{h} * c_j$, downsample by a factor of 2 in each dimension.

Compute $w_{j+1}^4 = \overline{h}\overline{g}\,\overline{g} * c_j$, downsample by a factor of 2 in each dimension.

Compute $w_{j+1}^5 = \overline{h}\overline{g}\,\overline{g} * c_j$, downsample by a factor of 2 in each dimension.

Compute $w_{j+1}^6 = \overline{g}\overline{h}\overline{g} * c_j$, downsample by a factor of 2 in each dimension.

Compute $w_{j+1}^7 = \overline{h}\,\overline{h}\overline{g} * c_j$, downsample by a factor 2 in each dimension.

The wavelet function is defined as the difference between the scaling functions of two successive scales:

$$\tfrac{1}{8}\psi\left(\tfrac{x}{2}, \tfrac{y}{2}, \tfrac{z}{2}\right) = \phi(x, y, z) - \tfrac{1}{8}\phi\left(\tfrac{x}{2}, \tfrac{y}{2}, \tfrac{z}{2}\right). \tag{18}$$

This choice of wavelet function will allow for a very simple reconstruction formula, where the original data cube can be recovered by simple co-addition of the wavelet coefficients and the last smoothed approximation. Furthermore, since the scaling function is chosen to be isotropic, the wavelet function is therefore also isotropic. Figure 3 shows an example of such a 3-D isotropic wavelet function.

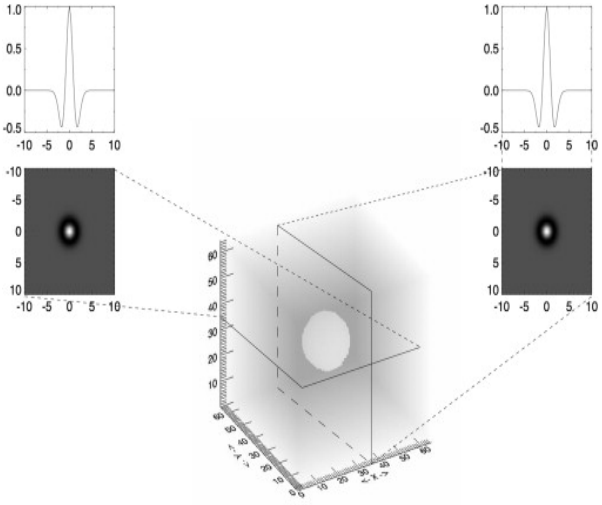

Figure 3. 3-D Isotropic wavelet function.

The implementation of the starlet transform relies on the very efficient *à trous* algorithm, whose name is derived from the French term meaning "with holes" (Holschneider *et al.* 1989); Shensa 1992. Let h be the filter associated with ϕ:

$$h[k,\ l,\ m] = h_{1D}[k]\, h_{1D}[l]\, h_{1D}[m], \tag{19}$$

$$h_{1D}[k] = [1,\ 4,\ 6,\ 4,\ 1]/16, \quad k \in [\![-2,\ 2]\!]\ ; \tag{20}$$

and let g be the filter associated with the wavelet ψ:

$$g[k,\ l,\ m] = \delta[k,\ l,\ m] - h[k,\ l,\ m]. \tag{21}$$

The *à* trou algorithm defines for each j a scaled version $h_{1D}^{(j)}$ of the 1-D filter h_{1D} such that

$$h_{1D}^{(j)}[k] = \begin{cases} h_{1D}[k] & \text{if } k \in 2^j\mathbb{Z} \\ 0 & \text{otherwise} \end{cases}. \tag{22}$$

For example, we have

$$h_{1D}^{(1)} = [\ldots, h_{1D}[-2],\ 0,\ h_{1D}[-1],\ 0,\ h_{1D}[0],\ 0,\ h_{1D}[1],\ 0,\ h_{1D}[2], \ldots \tag{23}$$

Due to the separability of h, for each j, we also can define

$$h^{(j)}[k,\ l,\ m] = h_{1D}^{(j)}[k]\, h_{1D}^{(j)}[l]\, h_{1D}^{(j)}[m] \tag{24}$$

$$g^{(j)}[k,\ l,\ m] = \delta[k,\ l,\ m] - h_{1D}^{(j)}[k]\, h_{1D}^{(j)} h_{1D}^{(j)}[m]. \tag{25}$$

From the original data cube c_0, the wavelet and approximation coefficients now can be extracted recursively using the filters $h^{(j)}$ and $g^{(j)}$:

$$c_{j+1}[k,\ l,\ m] = \left(\overline{h}^{(j)} * c_j\right)[k,\ l,\ m] \\ = \sum_{p,q,r} h_{1D}[p]\, h_{1D}[q]\, h_{1D}[r]\, c_j\left[k + 2^j p,\ l + 2^j q,\ m + 2^j r\right] \tag{26}$$

$$w_{j+1}[k,\ l,\ m] = \left(\overline{g}^{(j)} * c_j\right)[k,\ l,\ m]. \\ = c_j[k,\ l,\ m] - \sum_{p,q,r} h_{1D}[p]\, h_{1D}[q]\, h_{1D}[r]\, c_j\left[k + 2^j p,\ l + 2^j q,\ m + 2^j r\right] \tag{27}$$

Finally, due to the choice of wavelet function, the reconstruction is obtained by a simple co-addition of all the wavelet scales and the final smooth subband:

$$c_0[k,\ l,\ m] = c_J[k,\ l,\ m] + \sum_{j=1}^{J} w_j[k,\ l,\ m]. \tag{28}$$

The algorithm for the 3-D starlet transform is provided in Algorithm 2.

At each scale j, the starlet transform provides only one subband w_j instead of the seven subbands produced by the biorthogonal transform. However, since the subbands are not decimated in this transform, each w_j has exactly the same number of voxels as the the input data cube. The redundancy factor of the 3-D starlet transform, therefore, is J +1, where J is the number of scales. Although higher than the redundancy factor of the biorthogonal transform (equal to 1), the starlet transform offers a far reduced redundancy compared to a standard Undecimated Wavelet Transform (UWT; an undecimated version of the DWT introduced in the previous section, see (Starck, Murtagh, and Fadili (2010)), which would have a redundancy factor of $7J + 1$.

Read full chapter

URL: https://www.sciencedirect.com/science/article/pii/B9780128002650000035

Beyond Wavelets

M.N. Do, M. Vetterli, in Studies in Computational Mathematics, 2003

4.5 Numerical Experiments

Figure 4.15 shows an example image that is transformed by the PDFB implementing the discrete ridgelet transform. As we can see, the coefficients in the transform domain are very sparse – significant coefficients are located around edges *and* in the right directional subbands. With non-linear approximation using the PDFB, smooth regions are represented efficiently by the small size lowpass image while smooth edges are efficiently represented by a few directional local coefficients.

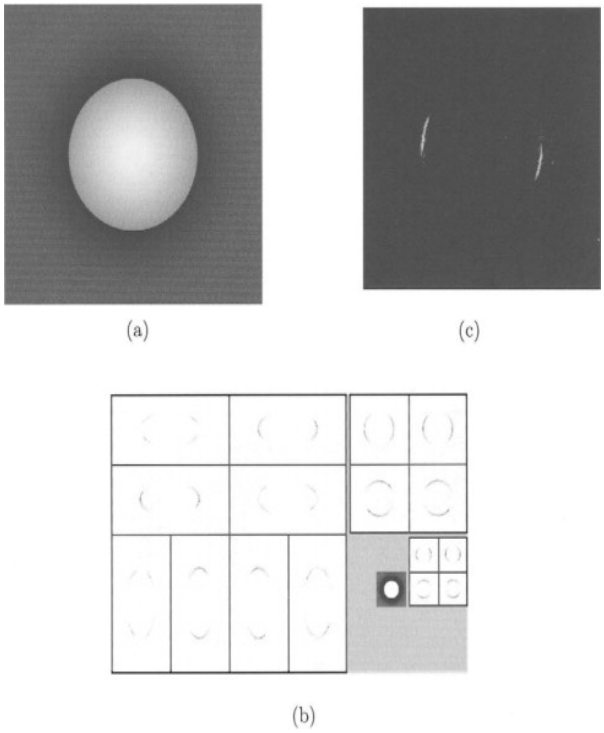

Figure 4.15. Example of PDFB. (a) Input image, (b) Magnitudes of PDFB coefficients, (c) Reconstruction from one PDFB subband. The LP uses the biorthogonal "9-7" filters, while the DFB's use the biorthogonal "23-45" quincunx filters designed by Phoong et al. [24] with support sizes equal to 23 × 23 and 45 × 45.

For comparison, Starck et al. [9] describe a different approach for the digital curvelet transform, in which they directly "discretize" the continuous definition. Their implementation uses the discrete Radon transform on image blocks, and thus the number of represented directions, which equals the block size, is reduced by half for every finer scale. This is unlike the curvelet construction in continuous space, or our construction. Furthermore, there is a redundancy factor equal to $16J + 1$ in their implementation compared with 1.33 in ours.

We now evaluate the non-linear approximation performance of the PDFB that implements the discrete curvelet transfrom and compare it with the performance by the 2-D discrete wavelet transform (DWT2). In these NLA experiments, for a given value M, we select the M-most significant coefficients in each transform domain, and then compare the reconstructed images from these sets of M coefficients. The wavelet transform used in the experiments is a biorthogonal transform with the "9-7" filters [25, 26] and 6 decomposition levels. The PDFB also uses the "9-7" filters in the LP decomposition. While the DFB in the PDFB uses the "23-45" biorthogonal quincunx filters designed by Phoong et al. [24]. The number of decomposition levels by the DFB at the finest pyramidal scale is 5, which leads to 32 directions.

Note that in this case, both the DWT2 and the PDFB transforms share the same multiscale detailed subspaces W_j as defined in Section 4.4.1, which are generated by the "9-7" lowpass filters. The difference is that in the DWT2, each subspace W_j is represented by a basis with three directions, whereas in the PDFB it is represented by a redundant frame with many more directions. Since the two transforms share the same detailed subspaces, it is possible to restrict the comparison in these subspaces. We expect that most of the refinement actions would happen around the image edges. Figure 4.16 and Figure 4.17 show sequences of non-linear approximated images at the finest subspace W_j using the DWT2 and the PDFB, respectively. We observe that the wavelet scheme slowly refines the detailed image

by isolated “dots” along the contours, while the contourlet scheme quickly refines by well-adapted “sketches”. The improvement by the PDFB can be seen both in terms of visual quality and reconstruction error. Finally, Figure 4.18 shows a detailed comparison of two non-linear approximated images by the DWT2 and the PDFB. We clearly see that fine contours (directional textures on cloths) are better represented by the contourlet transform compared to the wavelet transform. For more experimental results, we refer to [27].

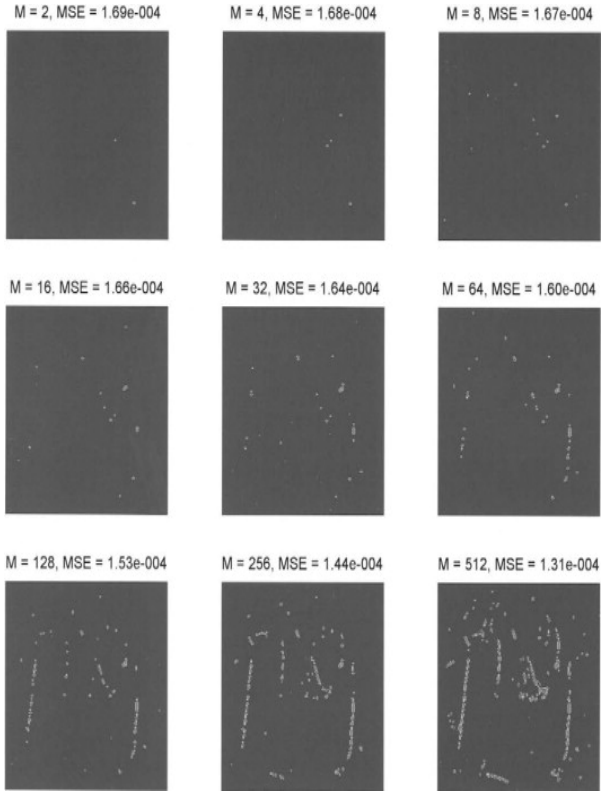

Figure 4.16. Sequence of images showing the non-linear approximation at the finest scale of the DWT2. M is the number of the most significant coefficients; MSE is the mean square error against the input image into the finest detailed subspace. The input is the “Peppers” image.

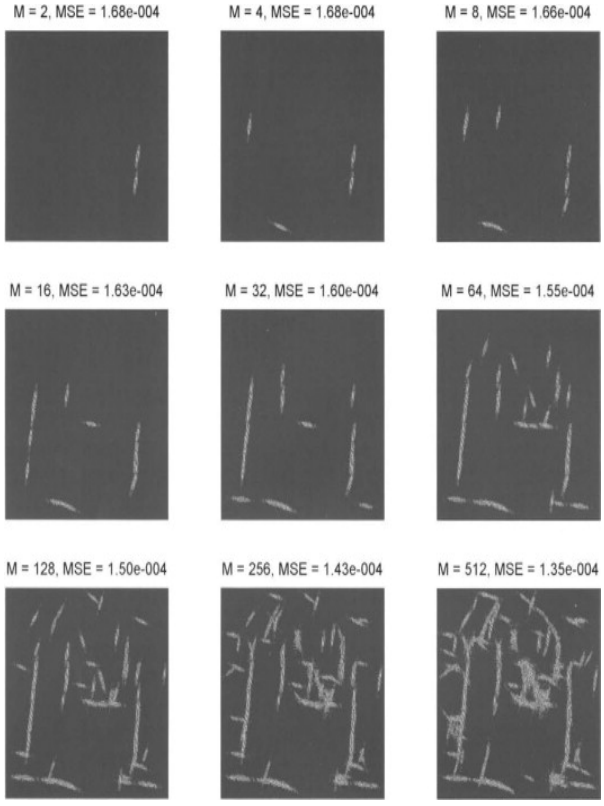

Figure 4.17. Same as in Figure 4.16 but with the PDFB. Note that the PDFB shares the same detailed subspace with the DWT2.

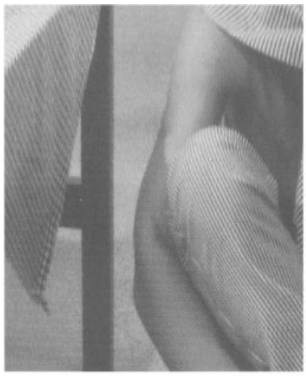

(a) Original image

(b) DWT2: PSNR = 24.34 dB

(c) PDFB: PSNR = 25.70 dB

Figure 4.18. Detail of non-linear approximated images by the DWT2 and the PDFB. In each case, the image originally of size 512 × 512 is reconstructed from the 4096-most significant coefficients in the transform domain.

Read full chapter

URL: https://www.sciencedirect.com/science/article/pii/S1570579X03800320